Ann. Geophys. Discuss., https://doi.org/10.5194/angeo-2019-36
Manuscript under review for journal Ann. Geophys.
Discussion started: 25 March 2019

Impact of Gravity wave drag on the thermospheric circulation: Implementation of a nonlinear gravity wave parameterization in a whole atmosphere model

Yasunobu Miyoshi [1], Erdal Yiğit [2]

[1] Department of Earth and Planetary Sciences, Kyushu University, Fukuoka, Japan
[2] Department of Physics and Astronomy, Space Weather Lab, George Mason University, Fairfax, VA, USA

Correspondence to: Yasunobu Miyoshi (y.miyoshi.527@m.kyushu-u.ac.jp)

Abstract. To investigate the effects of the gravity wave (GW) drag on the general circulation in the thermosphere, a nonlinear GW parameterization that estimates the GW drag in the whole atmosphere system is implemented in a whole atmosphere general circulation model (GCM). Comparing the simulation results obtained with the whole atmosphere scheme with the ones obtained with a conventional linear scheme, we study the GW effects on the thermospheric dynamics for solstice conditions. The GW drag significantly decelerates the mean zonal wind in the thermosphere. The GWs attenuate the migrating semidiurnal solar tide (SW2) amplitude in the lower thermosphere, and modifies the latitudinal structure of the SW2 above 150 km height. The SW2 simulated by the GCM based on the nonlinear whole atmosphere scheme agrees well with the observed SW2. The GW drag in the lower thermosphere has zonal wavenumber 2 and semidiurnal variation, while the GW drag above 150 km height is enhanced in high latitude. The GW drag in the thermosphere is a significant dynamical and plays an important role in the momentum budget of the thermosphere. Therefore, a GW parameterization accounting for thermospheric processes is essential for coarse-grid whole atmosphere GCMs in order to more realistically simulate the atmosphere-ionosphere system.

1 Introduction

It has been widely recognized that internal atmospheric waves from the lower atmosphere, such as planetary waves, solar tides and gravity waves (GWs), propagate into the upper atmosphere and affect the circulation in the thermosphere-ionosphere system (Yiğit and Medvedev, 2015, and references therein). In this study, we focus our attention on the impact of GWs of lower atmospheric origin on the thermospheric circulation. Due to insufficient observations of the neutral wind in the thermosphere, behaviour of GWs in the thermosphere has not been sufficiently known. Recently, an increasing number of numerical studies have revealed direct upward propagation of GWs from the lower atmosphere into the thermosphere and demonstrated significant GW effects on the thermospheric circulation (e.g., Yiğit et al., 2014; Heale et al., 2014; Gavrilov and Kshevetskii, 2015). Earlier, using a regional model and ray-tracing method, Vadas and Fritts (2004) showed that GWs generated by cumulus convection can propagate into the thermosphere and produce large GW drag in the thermosphere.

Ann. Geophys. Discuss., https://doi.org/10.5194/angeo-2019-36
Manuscript under review for journal Ann. Geophys.
Discussion started: 25 March 2019

GWs with high frequency (large vertical wavelength) can penetrate into the thermosphere (Vadas and Fritts, 2005). Yiğit et al. (2008) developed a nonlinear whole atmosphere GW parameterization, and succeeded in the implementation and application of their GW parameterization in the Coupled Middle Atmosphere Thermosphere-2 (CMAT2) general circulation model (GCM). Yiğit et al. (2009) showed that the dynamical effects of gravity waves in the thermosphere are comparable with the ion drag effects up to ionospheric F2 region altitudes. Later, based on the similar modeling framework, Yiğit and Medvedev (2009) showed for the first time that GW thermal effects are very important globally in the thermosphere and compete with Joule heating. More recently, Yiğit and Medvedev (2017) demonstrated that the small-scale GWs impact the amplitude of the diurnal tide in the low-latitude middle atmosphere and in the high-latitude thermosphere. Based on idealized numerical simulations with the Yiğit et al. (2008) scheme, Medvedev et al., (2017) have discovered that the magnetic field configuration can significantly influence the propagation and dissipation of lower atmospheric GWs in the thermosphere via the ion drag force.

GW effects can also be studied using high-resolution GCMs. Models are increasingly capable of implementing higher resolutions, which can capture smaller scale physics. Using a GW-resolving (i.e., high horizontal resolution) GCM, Miyoshi and Fujiwara (2008) and Miyoshi et al. (2014, 2015) investigated upward propagation of GWs and the GW drag in the thermosphere. They indicated that the GW drag in the thermosphere is much larger than that in the mesopause region. The GW activity in the thermosphere is stronger in winter than in summer and is correlated with the strength of the strato-mesospheric jet. Overall, high-resolution simulations supported the finding that the mean GW effects in the thermosphere can be adequately represented by physics-based GW parameterizations, such as the one developed by Yiğit et al. (2008).

These numerical studies indicated that the GW drag plays an important role in maintaining the momentum and energy balance in the thermosphere. Both GW parameterizations and high-resolution simulations provide various advantages as well as some limitations. While, the mean global structure of GW effects is well represented by GW parameterizations extending into the thermosphere, high-resolution simulations can more self-consistently simulate GW processes probably in more detail, for example, smaller-scale variability in GWs can be better captured. This implies overall that a GW resolving GCM is necessary in order to simulate the themopheric circulation more accurately. However, numerical diffusion schemes may excessively damp smaller scale GWs. Also, conducting numerical simulations with a GW-resolving GCM requires high performance computer systems and overall needs much more computational time and data storage. Therefore, long-term simulations using a GW-resolving GCM is unpractical. Therefore, a low-resolution GCM based on a physics-based whole atmosphere GW parameterization is strongly required. However, there are only a few studies concerning GW drag parameterization for the thermosphere and there are various aspects of GW effects in the thermosphere that are still unexplored. One such unexplored territory that is the focus of this paper is the interaction of GWs with the semidiurnal migrating tide in the upper atmosphere. Simultaneously, this work serves as the first study with the Kyushu University Whole Atmosphere GCM implementing the whole atmosphere GW parameterization by Yiğit et al. (2008). So, we will also study and revisit the mean GW effects on the thermosphere.

The descriptions of the GCM, the GW parameterization, and of numerical simulations are presented in section 2. Results and Discussion are presented in section 3. Concluding remarks follow in section 4.

2 General Circulation Model, Gravity Wave Schemes, and Experiment Design

The model used in this study is a whole atmosphere GCM as shown in Miyoshi and Fujiwara (2003, 2006, 2008). This model is a thermospheric extension of the middle atmosphere model developed at Kyushu University (Miyahara et al., 1993; Miyoshi, 1999). The GCM is a global spectral model with a horizontal grid spacing of 2.8° latitude × 2.8° longitude. The GCM has 150 layers with a vertical resolution of 0.2 scale heights. The GCM covers the region from the ground to the exobase. It has a complete set of physical processes appropriate for the whole atmosphere region. The GCM is the same as the neutral atmospheric part of an atmosphere-ionosphere coupled model GAIA (Ground-to-topside model of Atmosphere and Ionosphere for Aeronomy; Jin et al., 2008, 2011).

The GCM incorporates schemes for a hydrological cycle, a boundary layer, moist convection, and infrared and solar radiations (Miyoshi and Fujiwara, 2003, 2006). Effects of mountains and land-sea-contrast are also taken into account. In the thermosphere, the GCM has schemes for molecular diffusion, thermal conductivity, Joule heating, ion-drag force, and auroral precipitation heating. To estimate Joule heating, ion-drag force, and auroral precipitation heating, the electron density are prescribed using an empirical ionosphere model. The global electron density distribution produced by the solar radiation is represented by the Chiu's empirical model (Chiu, 1975). Electrons produced by auroral particles are estimated by Fuller-Rowell and Evans (1987). We use a coarse grid in this study, which provides computational efficiency, and represent GWs that are not explicitly resolved by the model with orographic and nonorographic GW parameterizations. The GW parameterization developed by McFarlare (1987) is used for orographic GWs. The previous standard version of the GCM includes a linear nonorographic GW parameterization developed by Lindzen (1981). However, the GW drag estimated by these GW parameterizations are taken into account only below 100 km height. Thus, note that no GW effects are calculated in the thermosphere above 100 km height in this configuration. This setup mimics the traditional approach of accounting for GWs only in the middle atmosphere, which is essentially what low-top middle atmosphere models used to do. The numerical simulation using this original GCM is called EXP1. This standard version is described in detail in previous publications (Miyoshi and Fujiwara, 2003, 2006; Miyoshi et al., 2009).

To assess impacts of GW drag on the general circulation in the thermosphere as well as in the lower and middle atmosphere, we need a GW scheme that extends into the thermosphere. Therefore, the GW parameterization developed in the work by Yiğit et al., (2008) has been implemented in the GCM developed by Miyoshi and Fujiwara (2003). Yiğit's GW parameterization can estimate the GW effects in the whole atmosphere system from the troposphere to the upper thermosphere. The GW spectrum is specified in terms of momentum fluxes as a function of horizontal phase speeds. The phase speeds of GWs used in GW calculations range from 2 m s^{-1} to 80 m s^{-1}. The peak GW flux at the source level and the horizontal wavenumber are set at 0.00025 m^2 s^{-2} and 2π/250 km^{-1}, respectively (see Figure 1 of Yiğit et al., 2012 for a

Ann. Geophys. Discuss., https://doi.org/10.5194/angeo-2019-36
Manuscript under review for journal Ann. Geophys.
Discussion started: 25 March 2019

representative GW spectrum). Dissipation of gravity waves due to nonlinear interactions (Medvedev and Klaassen, 2000), radiative damping, molecular diffusion and thermal conduction, eddy viscosity and ion drag are taken into account. This scheme has been used successfully in different Earth modeling frameworks (e.g., Lübken et al, 2018) and also for Mars atmosphere (Yiğit et al., 2018). The numerical simulation with Yiğit's whole atmosphere parameterization is called EXP2. The GCM used in EXP1 is identical to the GCM used in EXP2 except for the nonorographic GW parameterization. Namely, in EXP2, Lindzen's GW parameterization, which cuts off GW effects at around 100 km, is replaced by Yiğit's GW parameterization, which calculates GW effects in the entire atmosphere. By comparing EXP1 and EXP2, we investigate the impact of the GW drag on the general circulation in the middle and upper atmospheres by comparing EXP1 and EXP2.

To exclude influences from temporal variations in solar UV/EUV fluxes and geomagnetic activity, we performed the numerical simulations under solar minimum and geomagnetically quiet conditions. The 10.7 cm solar radio flux (F10.7) was fixed at 70×10^{-22} W m^{-2} Hz^{-1}, and the cross polar potential was set at 30 kV during the numerical simulations. Numerical simulations was conducted under June solstice conditions. The data were sampled at 1 h intervals in June.

3 Results and Discussions

3.1 Zonal mean zonal wind

Impacts of GWs on the zonal mean zonal wind are examined first. Figure1a shows height–latitude section of the zonal and diurnal mean zonal wind obtained by the application of the Lindzen scheme (EXP1). Data are averaged from 1 June to 30 June. Note that thermospheric GW effects above 100 km height are not incorporated in this scheme. Strong jets exist in the stratosphere and mesosphere. These jets weaken in the upper mesosphere, and the reversal of the zonal wind direction occurs around 80–100 km height. It is well known that this reversal of the zonal wind is generated by the GW drag (e.g., Lindzen 1981, Matsuno 1982, Garcia and Solomon, 1985). Again, the westward (eastward) wind appears above 120 km height in the Northern Hemisphere (Southern) Hemisphere. The peak of the westward wind (48–52 m s^{-1}) above 120 km is located at 50° N, whereas the peak of the eastward wind (20–25 m s^{-1}) above 120 km height appears at 30° S.

Figure 1b shows the zonal and diurnal mean zonal wind distribution obtained by the application of the Yiğit scheme (EXP2). As shown before, Yiğit's GW parameterization is implemented in the whole atmosphere region. The strato-mesospheric jets weaken in the upper mesosphere, and the reversal of the zonal wind direction occurs at 80–100 km height. Above 120 km height, the westward and eastward winds are dominant in the Northern and Southern Hemispheres, respectively. These features obtained in EXP2 are the same as those in EXP1. However, the reversal of the zonal wind direction at 80–100 km height is much clearer in EXP2 than in EXP1. The peak values of the zonal mean zonal wind above 120 km height are weaker in EXP2 than in EXP1. These results indicate that including GW effects above 100 km height affects the magnitude of the zonal mean zonal wind and provides a deceleration mechanism.

1.2 Migrating Semidiurnal Tide

The migrating semidiurnal tide (SW2) is examined next. Figure 2a shows the height–latitude distribution of the temperature component of the SW2 amplitude in June obtained by EXP1. The amplitude maximizes around 125 km height. The maxima are 41 K at 15° S and 12 K at 20° N. The peak of the SW2 amplitude above 200 km height (34 K) appears at 15–25° S, and the secondary peak (10 K) is found around 45° N. Using the SABER (Sounding of the Atmosphere using Broadband Emission Radiometry) measurement on board the TIMED (Thermosphere Ionosphere Mesosphere Energetics Dynamics) satellite, Forbes et al. (2008) investigated behavior of the SW2 in the mesosphere and lower thermosphere (MLT). The SW2 amplitude at 110 km height observed by the SABER instrument has peak values of about 15–20 K at 10–20° S and at 20–25° N, while peak values at 110 km height in EXP1 are about 30–35 K. The SW2 in EXP1 is much larger than the observation. Forbes et al. (2011) investigated seasonal variation of the SW2 in the upper thermosphere using the CHAMP (Challenging Minisatellite Payload) and GRACE (Gravity Recovery and Climate Experiment) accelerometer measurements. The observed SW2 in June also has two peaks (15-20° S and 40° N), and the peak value during solar minimum is 24 K (Figures 7 and 8 of Forbes et al., 2011). The simulated SW2 in the Southern (Northern) Hemisphere is larger (smaller) than the observed SW2.

Figure 2b shows the temperature component of the SW2 amplitude obtained by EXP2. The SW2 in the lower thermosphere maximizes at 15–20° S and at 20° N. The SW2 peaks at 100–200 km height moves southward in EXP2. The SW2 amplitude in the lower thermosphere in EXP2 is weaker than the one in EXP1 by about 20–40 % (Figure 2c). Results obtained with EXP2 compares better with the observed SW2 amplitude. Above 200 km height, the SW2 amplitude in EXP2 maximizes at 10° S (25 K), and secondary peak is found at 40° N (15–20 K). The SW2 amplitude in the Southern (Northern) Hemisphere is weaker (stronger) in EXP2 than in EXP1. This means that the latitudinal structure of the SW2 above 200 km height is modified by GW propagating and dissipation in the middle and upper thermosphere. Moreover, the SW2 in the upper thermosphere obtained by EXP2 agrees well with the observed SW2 amplitude. Figures 3a and 3b show the zonal wind component of the SW2 amplitude in EXP1 and EXP2, respectively. Figure 3c shows the amplitude difference between the EXP1 and EXP2. The maximum of the zonal wind component of the SW2 at 120 km height in EXP1 (EXP2) is 68 (55) m s^{-1}. The GW parameterization attenuates the zonal wind component of the SW2 in the lower thermosphere. Moreover, above 200 km height, the GW parameterization modifies the latitudinal structure of the zonal wind component. The effects of the GW drag on the migrating diurnal tide in the MLT was studied by Miyahara and Forbes (1991). They showed that the DW1 is attenuated by the GW drag. Yiğit and Medvedev (2017) investigated the effects of GWs on the diurnal tide from the mesosphere to the upper thermosphere. They found that while GWs enhance the tidal amplitude in the MLT, GWs can both damp and strengthen the tides in the thermosphere. On the other hand, the present results indicate the GW drag has widereaching implications for the migrating tides. Namely GWs attenuate the SW2 amplitude in the MLT region, improving model simulations with respect to observations. Overall, this is the most dominant effect of the GW drag on the SW2.

3.3 Zonal mean of the zonal GW drag

Figure 4a shows the height–latitude section of the zonal and diurnal mean of the zonal GW drag estimated by Lindzen's parameterization (EXP1). Eastward (westward) acceleration exists in the Northern (Southern) Hemisphere, and attenuates the mesospheric jet. Figure 4b shows the zonal and diurnal mean of the zonal GW drag estimated by Yiğit's parameterization (EXP2). The distribution of the zonal GW drag at 60–90 km height in EXP2 is similar to that in EXP1. However, the GW drag in EXP2 extends to 300 km height. It is noteworthy that the magnitude of the GW drag in 150–300 km height is comparable to that in the MLT region.

3.4 Longitudinal variation of the GW drag at 35° N

In the previous sections, we investigate zonal and diurnal mean of the GW drag. Longitudinal and diurnal variabilities of the winds are significant in the thermosphere, so that longitudinal/diurnal variability of the GW drag is examined next. Figure 5a shows height-longitude distribution of the zonal GW drag at 35° N, where the SW2 amplitude maximizes in the lower thermosphere. The zonal GW drag in Figure 5a is averaged between 00 UT and 01 UT. The GW drag at 70–100 km height is eastward at all longitudes, and contribute the attenuation and reversal of the westward jet in the upper mesosphere.

The zonal and diurnal mean of the zonal GW drag at 35° N in the 100–200 km height region is smaller than 20 m s^{-1} (day)$^{-1}$ (Figure 4b). However, Figure 5a indicates that the GW drag can range from –100 m s^{-1} (day)$^{-1}$ to 200 m s^{-1} (day)$^{-1}$ within the one-hour period. The maximum acceleration is located at 157° E and 150 km height. The GW drag has zonal wavenumber 2 structure in the 100–200 km height region, and the peak of the GW drag descends with increasing longitude. Figure 4b shows height-longitude section of the zonal wind at 35 N° averaged between 00 UT and 01 UT. The zonal wind distribution in the 100–200 km height region has also zonal wavenumber 2 structure, and descends with increasing longitude, indicating characteristics of the upward propagating SW2. The eastward (westward) acceleration of GW drag in the 100–200 km region occurs in the region of westward (eastward) wind. It is clearly seen that the GW drag attenuates the zonal wind variation associated with the SW2. Thus, the attenuation of the SW2 in EXP2 is explained by dissipating GWs as represented by Yiğit scheme. The main dissipation mechanism of GWs in the thermosphere are due to ion drag, molecular diffusion and thermal conduction, while in the MLT region nonlinear interactions play an important role.

Figure 6a and 6b show the global distribution of the zonal GW drag at 120 km at two representative times, 00–01 UT and at 06–07 UT, respectively. The GW drag in low and middle latitudes has zonal wavenumber 2 structure. The magnitude of the GW drag sometimes exceeds 150 m s^{-1} (day)$^{-1}$. The distribution of GW drag in 00–01 UT is clearly out of phase with that in 06–07 UT, indicating semidiurnal variation of the GW drag. In the work by Miyoshi and Fujiwara (2014), the relationship between GW drag and SW2 was investigated using a GW-resolving GCM. They showed that the semidiurnal variation of the GW drag is significant in the lower thermosphere and it decelerates the background zonal wind variation. The present result is consistent with the result obtained by Miyoshi and Fujiwara (2014).

3.5 Longitudinal Variation of the GW Drag at High Latitudes

In this section, the relationship between the GW drag and the zonal wind in high latitudes, where the diurnal variation of the zonal wind is significant, is investigated. Figure 7a shows height–longitude section of the zonal GW drag in EXP2 at 65° N in 00–01 UT. Eastward acceleration is dominant in the 60–110 km height region, which attenuates the westward wind. Above 150 km height, zonal wavenumber 1 structure is dominant. Eastward acceleration (westward acceleration) appears in 0–180° E (180–360° E) longitude sector. Studying the GW drag together with the zonal wind (EXP2) distribution shown in Figure 7b shows that the GW drag is predominantly directed against the zonal wind and thus tends to decelerate the wind. It is noteworthy that the magnitude of eastward acceleration at 130–270 km height is a few hundred m s^{-1} (day) $^{-1}$, and the maximum values of –650 m s^{-1} (day) $^{-1}$ is found at 275° E and 230 km height.

To investigate the impact of the GW drag on the zonal wind variation, the zonal wind distribution obtained by EXP1 is shown in Figure 7c. In EXP1, the westward (eastward) wind prevails in 0–180° (180–360°) longitude sector above 150 km height. Figure 7d shows the difference of the zonal wind between EXP2 and EXP1 (EXP2–EXP1). This essentially shows the difference between the impact of the GW effects on the zonal circulation represented by two different schemes. It is noteworthy that the differences are substantial not only above 100 km, where EXP1 does not include any GW drag, but also in the mesosphere. Both the westward and eastward wind above 150 km height are 10–30 m s^{-1} smaller in EXP2 than in EXP1. This means that the GW drag attenuates the amplitude of the wave number 1 structure of the zonal wind. The difference of the zonal wind in the mesosphere is mainly caused by the substantial differences of the treatment of the GW process. This differences will be discussed in section 3.6.

The global distribution of the zonal GW drag at 200 km height is examined here. Figure 8a and 8b show the zonal GW drag distribution in 00–01 UT and 06–07 UT, respectively. In both figures, the GW drag is significant at high latitudes. For example, in 00–01 UT, westward acceleration of 1500 m s^{-1} (day) $^{-1}$ is found at 40–50° E and 80° N, while eastward acceleration of –1200 m s^{-1} (day) $^{-1}$ appears at 275° E and 70° N. These strong GW drag regions move westward with time, and westward acceleration of –1200 m s^{-1} (day) $^{-1}$ appears at 170° E and 80° N in 06–07 UT. The magnitude of the GW drag in high latitudes is comparable to the magnitude of the ion-drag force (e.g., Yiğit et al., 2012; Miyoshi et al, 2014).

Figure 8c and 8d show the horizontal wind distribution at 200 km height in 00–01 UT and 06–07 UT, respectively. Color shading in Figures 8a and 8b shows the zonal wind distribution. The enhanced zonal GW drag is located at the regions where the strong zonal wind appears. The strong zonal winds in high latitudes ~~is~~ are mainly generated by the convective electric fields of magnetospheric origin, auroral energy precipitation, and ion-neutral coupling processes such as ion drag force and Joule heating (e.g., Yigit and Ridley, 2011). The enhanced eastward (westward) wind is favorable for upward propagation of westward (eastward) moving GWs from the lower atmosphere. The westward (eastward) acceleration due to the dissipation/breaking of westward moving (eastward) GWs occurs in the eastward (westward) wind region. This is the reason why the GW drag is enhanced at high latitudes. These results indicated that the GW drag plays an important role on the momentum budget in high latitudes around 200 km height. Using a GW-resolving GCM, Miyoshi and Fujiwara (2014) showed the enhancement of the GW drag in polar region at 200 km height. Their result is in good agreement with the results presented here.

3.6 Discussions

General circulation models (GCMs) provide a powerful methodology for studying the global effects of gravity waves (GWs) in the atmosphere. One strength is the continuous coverage of atmospheric layers, thus interaction processes between different layers can be studied. However, they have limited resolutions so physical parameterizations are crucial. Nowadays, atmospheric models are gradually being converted into whole atmosphere models, which can provide a framework in which atmospheric wave propagation can be studied from the lower atmosphere to the upper atmosphere in a more self-consistent manner. Also, it is increasingly acknowledged that GW parameterizations must cover the entire atmosphere, following the realization that GWs deposit their energy and momentum at different layers in the atmosphere with a significant portion being deposited in the middle thermosphere. In this context, we exploit the capability of the whole atmosphere GW parameterization of Yiğit et al. (2008). Note that recent studies showed that lower atmospheric GWs can directly propagate into the thermosphere and can dump significant energy and momentum there. For example, the magnitude of the GW drag in the lower thermosphere sometimes exceeds 150 m s^{-1} (day)$^{-1}$, whereas the magnitude of the GW drag at 200 km height at high latitudes exceeds 1000 m s^{-1} (day)$^{-1}$. In summary, GWs can produce a variety of effects in the thermosphere, including dynamical (Yiğit et al., 2009), thermal (Yiğit and Medvedev, 2009; Hickey et al., 2011), and mixing effects (Walterscheid and Hickey, 2012). Transient atmospheric processes can dramatically modulate penetration of GWs into the thermosphere: During minor warming, thermospheric GWs activity can be enhanced significantly (e.g., Yiğit et al., 2014; Yiğit and Medvedev, 2016), while during major warmings it may encounter a decrease (Nayak and Yiğit, 2019). Here, we used a whole atmosphere GCM incorporating a whole atmosphere GW parameterization in order to the study the mean dynamical effects of GWs and their impact on the semidiurnal tides in the thermosphere.

Using the SABER (Sounding of the Atmosphere using Broadband Emission Radiometry) measurement on board the TIMED (Thermosphere Ionosphere Mesosphere Energetics Dynamics) satellite, Forbes et al. (2008) investigated behavior of the SW2 in the mesosphere and lower thermosphere (MLT). There, the typical observed peak values for the SW2 amplitudes are situated at low-latitudes during June solstice: 15–20 K at 10–20° S and at 20–25° N. In our study, GCM simulations based on two different GW parameterizations yield different results for the SW2 tide. While the simulation with the standard Lindzen scheme overestimate the tidal amplitude, the one with the Yiğit scheme matches observations better. This can be explained by the additional GW drag in the thermosphere (i.e., additional physics) as accounted for by the Yiğit scheme, which attenuates the zonal wind variation associated with the SW2.

Using the CHAMP (Challenging Minisatellite Payload) and GRACE (Gravity Recovery and Climate Experiment) accelerometer measurements, Forbes et al. (2011) showed the SW2 amplitude in the upper thermosphere. The GCM without

GW drag parameterization in the thermosphere fails to reproduce the observed SW2 in the upper thermosphere, whereas the GCM with the GW parameterization succeeds in reproducing the behaviour of the observed SW2 in the upper thermosphere. This result also indicates the importance of the GW effects in the thermosphere.

There are substantial differences between the linear and the nonlinear schemes in the treatment of GW processes as has been initially discussed in detail in the work by Yiğit et al (2008). One major difference is that the linear scheme is based on the linear saturation principle, ignoring wave-wave interactions, while the Yiğit scheme takes into account not only nonlinear wave-wave interactions but also dissipation of GWs due to additional processes, such as ion drag, molecular viscosity and thermal conduction are taken into account, which are important dissipative processes in the thermosphere-ionosphere system. Any GCM that is extending into the thermosphere, including a GW parameterization, must incorporate these effects on GW propagation. While the linear scheme assumes an artificial tuning factor for the GW drag, the nonlinear scheme does not require any artificial tuning parameters. However, GW parameterizations are not devoid of limitations. They all assume single-column approach and instantaneous response of the flow field to the upward propagating waves.

The whole atmosphere GCM uses an empirical ionospheric model. At high-latitudes, the behavior of the ionosphere can substantially influence the thermospheric circulation. On the other hand, the background atmosphere is very important for the GW propagation and dissipation. A modelling framework with self-consistent two-way coupled ionosphere-thermosphere system could provide a more realistic picture of ion-neutral coupling and GW effects could be evaluated more precisely at high-latitudes.

4. Concluding remarks

The GW parameterization developed by Yiğit et al. (2008) has been implemented in the Japanese Kyushu University whole atmosphere GCM (Miyoshi and Fujiwara, 2008), and the impact of small-scale GWs on the migrating semidiurnal tide as well as the GW effects on the general circulation of the thermosphere has been studied. We obtained the following results.

1. The GW drag attenuates the magnitude of the zonal/diurnal mean zonal wind in the thermosphere.

2. The GW drag attenuates the SW2 amplitude in the lower thermosphere, and modifies the latitudinal structure of the SW2 above 150 km height.

3. The GW drag in the lower thermosphere has zonal wavenumber 2 structure and have semidiurnal variation.

4. The GW drag above 150 km height is enhanced in high latitudes. The maximum value sometimes exceeds 1000 m s^{-1} $(day)^{-1}$. This means that the GW drag plays an important role on the momentum balance in high latitudes above 150 km height.

The whole atmosphere GCM used in this study uses an empirical ionosphere. Therefore, impacts of the GW drag on the ionospheric variability have not been investigated in this study. In the next step, implementation of GW drag parameterization in an atmosphere-ionosphere coupled model, such as GAIA (Jin et al., 2011) is strongly required. Using an atmosphere-ionosphere coupled model with GW drag, we will investigate impacts of the GW drag on the ionospheric variability.

Data Availability. Upon request, the data used for the publication of this study are available from Yasunobu Miyoshi (y.miyoshi.527@m.kyushu-u.ac.jp)

Author Contribution. YM performed the simulation and wrote a substantial portion of the paper. EY provided the whole atmosphere GW parameterization scheme, and significantly contributed to writing and discussion of results.

Competing interests. EY is one of the editors of this special issue. The authors declare that there are no conflicts of interests.

Acknowledgement. This work was supported by a JSPS Grant-in-Aid for Scientific Research grand numbers (B 15H03733) and (18H04447). The GFD/DENNOU library was used to produce the figures. The numerical simulation was performed using the computer system at Research Institute for Information Technology of Kyushu University, and at National Institute of Information and Communication Technology, Japan. E. Y. was partially funded by the National Science Foundation (NSF) grant AGS 1452137.

References

Chiu, Y. T.: An improved phenomenological model of ionospheric density, J. Atmos. Terr. Phys., 37, 1563-1570, 1975.

Forbes, J. M., Zhang, X., Palo, J., Russell, C., Mertens, J., and Mlynczak M.: Tidal variability in the ionospheric dynamo region, J. Geophys. Res., 113, A02310, doi:10.1029/2007JA012737, 2008.

Forbes, J. M., Zhang, X., Bruinsma, S. and Oberheide, J.: Sun-synchronous thermal tides in exosphere temperature from CHAMP and GRACE accelerometer measurements, J. Geophys. Res., 116, A11309, doi:10.1029/2011JA016855, 2011.

Fuller-Rowell, T. J., and Evans D. S.: Height-integrated Pedersen and Hall conductivity patterns inferred from the TIROS-NOAA satellite data, J. Geophys. Res., 92, 7606-7618, 1987.

Gavrilov, N. M., and Kshevetskii S. P.: Dynamical and thermal effects of nonsteady nonlinearacoustic-gravity wavespropagating from tropospheric sources to the upper atmosphere. Adv. Space Res., 56, 1833-1843, 2015.

Heale, C. J., Snively, J. B., Hickey, M. P., and Ali, C. J.: Thermospheric dissipation of upward propagating gravity wave packets, J. Geophys. Res., 119, doi:10.1002/2013JA019387, 2014.

Hickey, M. P., Walterscheid, R. L., and Schubert G.: Gravity wave heating and cooling of the thermosphere: Sensible heat flux and viscous flux of kinetic energy, J. Geophys. Res., 116, A12326, doi:10.1029/2011JA016792, 2011.

Jin, H., Miyoshi, Y., Fujiwara, H., Shinagawa, H.: Electrodynamics of the formation of ionospheric wave number 4 longitudinal structure. J. Geophys. Res. 113, A09307. http://dx.doi.org/10.1029/2008JA013301, 2008.

Jin, H., Miyoshi, Y., Pancheva, D., Mukhtarov, P., Fujiwara, H., and Shinagawa, H.: Response of migrating tides to the stratospheric sudden warming in 2009 and their effects on the ionosphere studied by a whole atmosphere-ionosphere model GAIA with COSMIC and TIMED/SABER observations, J. Geophys. Res., 117, A10323, doi:10.1029/2012JA017650, 2012.

Lindzen, R. S.: Turbulence and stress owing to gravity wave and tidal breakdown, J. Geophys. Res., 86, 9707– 9714, 1981.

Lübken, F.-J., Berger, U., and Baumgarten, G.: On the anthropogenic impact on long-term evolution of noctilucent clouds. Geophysical Research Letters, 45, 6681–6689, doi:10.1029/2018GL077719, 2018.

Matsuno, T.: A quasi one-dimensional model of the middle atmosphere circulation interacting with internal gravity waves, J. Meteorol. Soc. Jpn., 60, 215–226, 1982.

McFarlane, N. A.: The effect of orographically excited gravity wave drag on the general circulation of the lower stratosphere and troposphere, J. Atmos. Sci., 44, 1775– 1800, 1987.

Medvedev, A. S., Yiğit, E., and Hartogh, P.: Ion friction and quantification of the geomagnetic influence on gravity wave propagation and dissipation in the thermosphere-ionosphere, J. Geophys. Res.: Space Physics, 122. doi:10.1002/2017JA024785, 2017.

Medvedev A. S. and G. P. Klaassen: Parameterization of gravity wave momentum deposition based on nonlinear wave interactions: basic formulation and sensitivity tests, J. Atmos. Sol.-Terr. Phys., 10.1016/S1364-6826(00)00067-5, 62, 11, (1015-1033), 2000.

Miyahara, S., and Forbes, J. M.: Interactions between gravity waves and the diurnal tide in the mesosphere and lower thermosphere, J. Meteorological Society of Japan, 69,523-531, 1991.

Miyahara, S., Yoshida, Y., and Miyoshi, Y.: Dynamic coupling between the lower and upper atmosphere by tides and gravity waves, J. Atmos. Terr. Phy., 55, 1039-1053, 1993.

Miyoshi, Y.: Numerical simulation of the 5-day and 16-day waves in the mesopause region, Earth Planets Space, 51, 763-772, 1999.

Miyoshi, Y., and Fujiwara, H.: Day-to-day variations of migrating diurnal tide simulated by a GCM from the ground surface to the exobase, Geophys. Res. Lett., 30, 1789, doi:10.1029/ 2003GL017695, 2003.

Miyoshi, Y.: Temporal variation of nonmigrating diurnal tide and its relation with the moist convective activity, Geophys. Res. Lett., 33, L11815, doi:10.1029/2006GL026072, 2006.

Miyoshi, Y., and Fujiwara, H.: Gravity waves in the thermosphere simulated by a general circulation model, J. Geophys. Res., 113, D01101, doi:10.1029/ 2007JD008874, 2008.

Miyoshi, Y., Fujiwara, H., Forbes, J. M., and Bruinsma, S. L.: Solar terminator wave and its relation to the atmospheric tide, J. Geophys. Res., 114, A07303, doi:10.1029/2009JA014110, 2009.

Miyoshi, Y., Fujiwara, H., Jin, H., Shinagawa, H., and Liu, H.: Numerical simulation of the equatorial wind jet in the thermosphere, J. Geophys. Res., 117, A03309, doi:10.1029/2011JA017373, 2012.

Miyoshi, Y., Fujiwara, H., Jin, H., and Shinagawa H.: A global view of gravity waves in the thermosphere simulated by a general circulation model, J. Geophys. Res. Space Physics, 119, doi:10.1002/2014JA019848, 2014.

Miyoshi, Y., Fujiwara, H., Jin, H., and Shinagawa H.: Impacts of sudden stratospheric warming on general circulation of the thermosphere, J. Geophys. Res. Space Physics, 120, 10,897–10,912, doi:10.1002/2015JA021894, 2015.

Nayak, C., and Yiğit, E.: Variation of small-scale gravity wave activity in the ionosphere during the major sudden stratospheric warming event of 2009. J. Geophys. Res. Space Physics, 124, 470–488, doi: 10.1029/2018JA026048, 2019.

Vadas, S. L. and Fritts, D. C.: Thermospheric responses to gravity waves arising from mesoscale convective complexes, J. Atmos. Sol.-Terr. Phys., 66, 781–804, 2004.

Vadas, S. L., and Fritts D. C.: Thermospheric responses to gravity waves: Influences of increasing viscosity and thermal diffusivity, J. Geophys. Res., 110, D15103, doi:10.1029/2004JD005574, 2005.

Walterscheid, R. L., and Hickey M. P.: Gravity wave propagation in a diffusively separated gas: Effects on the total gas, J. Geophys. Res., 117, A05303, doi:10.1029/2011JA017451, 2012.

Yiğit, E., and Medvedev, A. S.: Heating and cooling of the thermosphere by internal gravity waves, Geophys. Res. Lett., 36, L14807, doi:10.1029/2009GL038507, 2009.

Yiğit, E. and Ridley A. J.: Effects of high-latitude thermosphere heating at various scale sizes simulated by a nonhydrostatic global thermosphere–ionosphere model, J. Atmos. Sol-Terr. Phys., 73(5-6), 592-600, doi:10.1016/j.jastp.2010.12.003, 2011.

Yiğit, E., and Medvedev, A. S.: Internal wave coupling processes in Earth's atmosphere, Adv. Space Res., 55, 983-1003, doi:10.1016/j.asr.2014.11.020, 2015.

Yiğit, E., and Medvedev, A. S.: Role of gravity waves in vertical coupling during sudden stratospheric warmings, Geosci. Lett., 3:27, doi: 10.1186/s40562-016-0056-1, 2016.

Yiğit, E., and Medvedev, A. S.: Influence of parameterized small-scale gravity waves on the migrating diurnal tide in Earth's thermosphere, J. Geophys. Res. Space Physics, 122, 4846–4864, doi:10.1002/2017JA024089, 2017.

Yiğit, E., Aylward, A. D., and Medvede, A. S.: Parameterization of the effects overtically propagating gravity waves for thermosphere general circulation models: Sensitivity study, J. Geophys. Res., 113, D19106, doi:10.1029/2008JD010135, 2008.

Yiğit, E., Medvedev, A. S., Aylward, A. D., Hartogh, P., and Harris, M. J.: Modeling the effects of gravity wave momentum deposition on the general circulation above the turbopause, J. Geophys. Res., 114, D07101, doi:10.1029/2008JD011132, 2009.

Yiğit, E., Medvedev, A. S., Ridley, A. J., Aylward, A. D., Harris, M. J., Moldwin, M. B., and Hartogh, P.: Dynamical effects of internal gravity waves in the equinoctial thermosphere, J. Atmos. Sol-Terr. Phys., 90-91, 104-116, 2012.

Yiğit, E., A. S. Medvedev, S. L. England, and T. J. Immel, Simulated variability of the high-latitude thermosphere induced by small-scale gravity waves during a sudden stratospheric warming, J. Geophys. Res. Space Physics, 119, doi:10.1002/2013JA019283, 2014.

Yiğit, E., Medvedev, A. S., and Hartogh, P.: Influence of gravity waves on the climatology of high-altitude Martian carbon dioxide ice clouds, Ann. Geophys., 36, 1631-1646., doi:10.5194/angeo-36-1631-2018, 2018.

Ann. Geophys. Discuss., https://doi.org/10.5194/angeo-2019-36
Manuscript under review for journal Ann. Geophys.
Discussion started: 25 March 2019

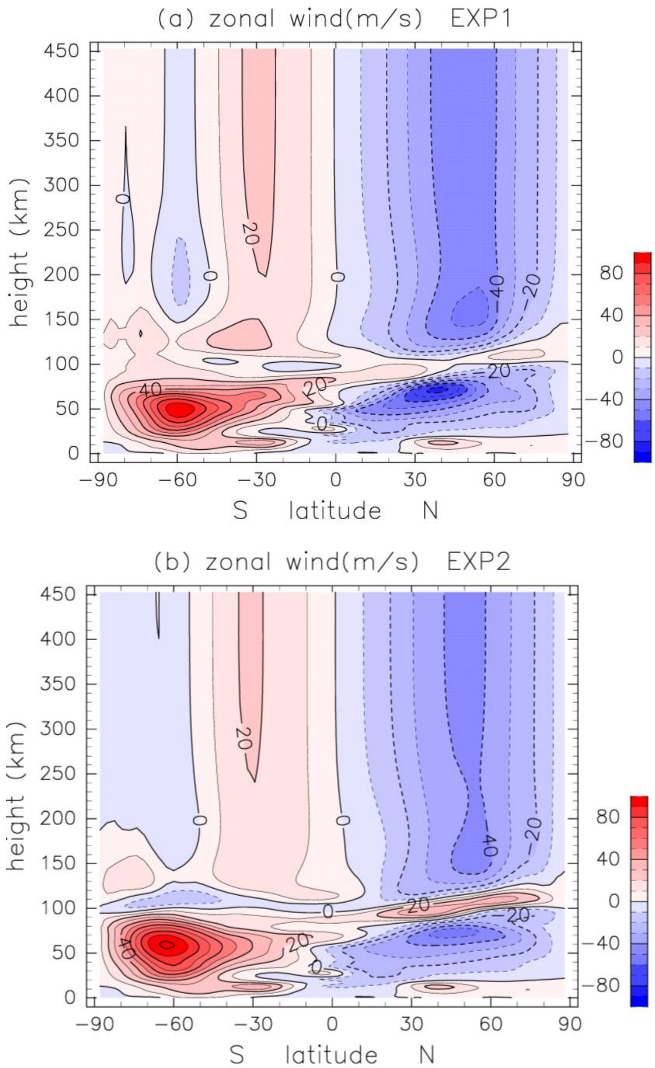

Figure1: (a) Height-latitude section of zonal and diurnal mean zonal wind obtained by EXP1 (the application of the Lindzen scheme below 100 km height). Data are averaged from 1 June to 30 June. Contour intervals of black lines are 10 m s^{-1}. Negative and positive values are eastward and westward winds, respectively. (b) As in Figure 1a except for the application of the Yiğit scheme in the whole atmosphere (EXP2).

Ann. Geophys. Discuss., https://doi.org/10.5194/angeo-2019-36
Manuscript under review for journal Ann. Geophys.
Discussion started: 25 March 2019

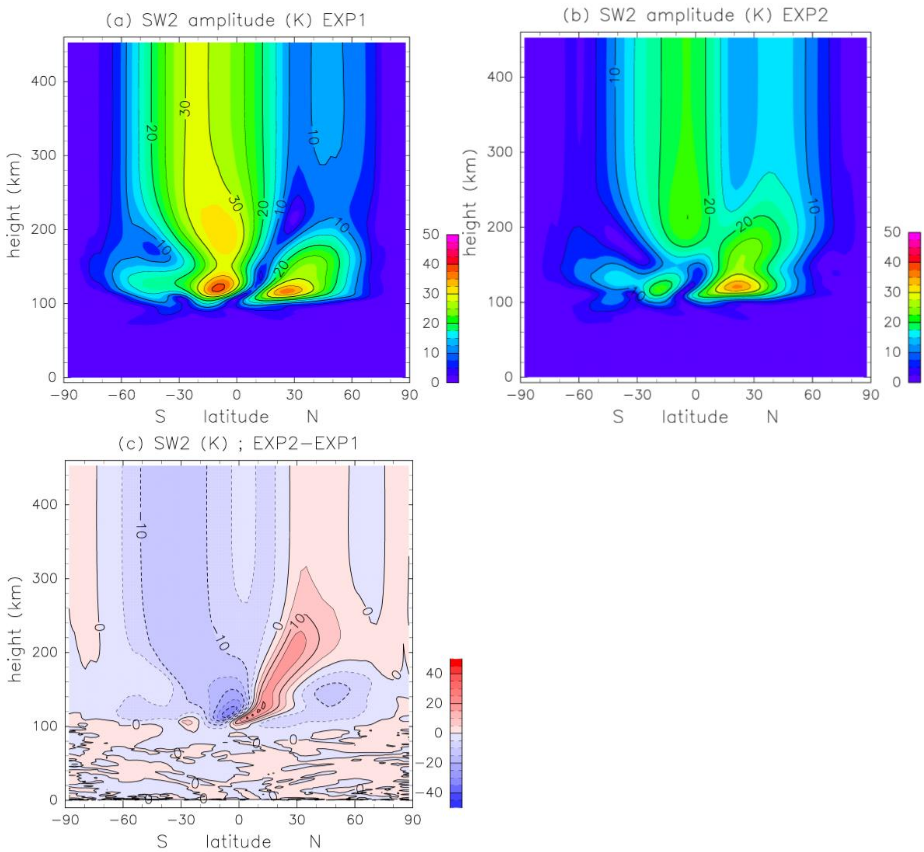

Figure2: (a) Height-latitude distribution of the temperature component of the SW2 amplitude in June obtained by EXP1. Units are K. Contour intervals are 5 K. (b)As in Figure 1a except for EXP2. (c) Temperature difference between EXP2 and EXP1 (EXP2–EXP1).

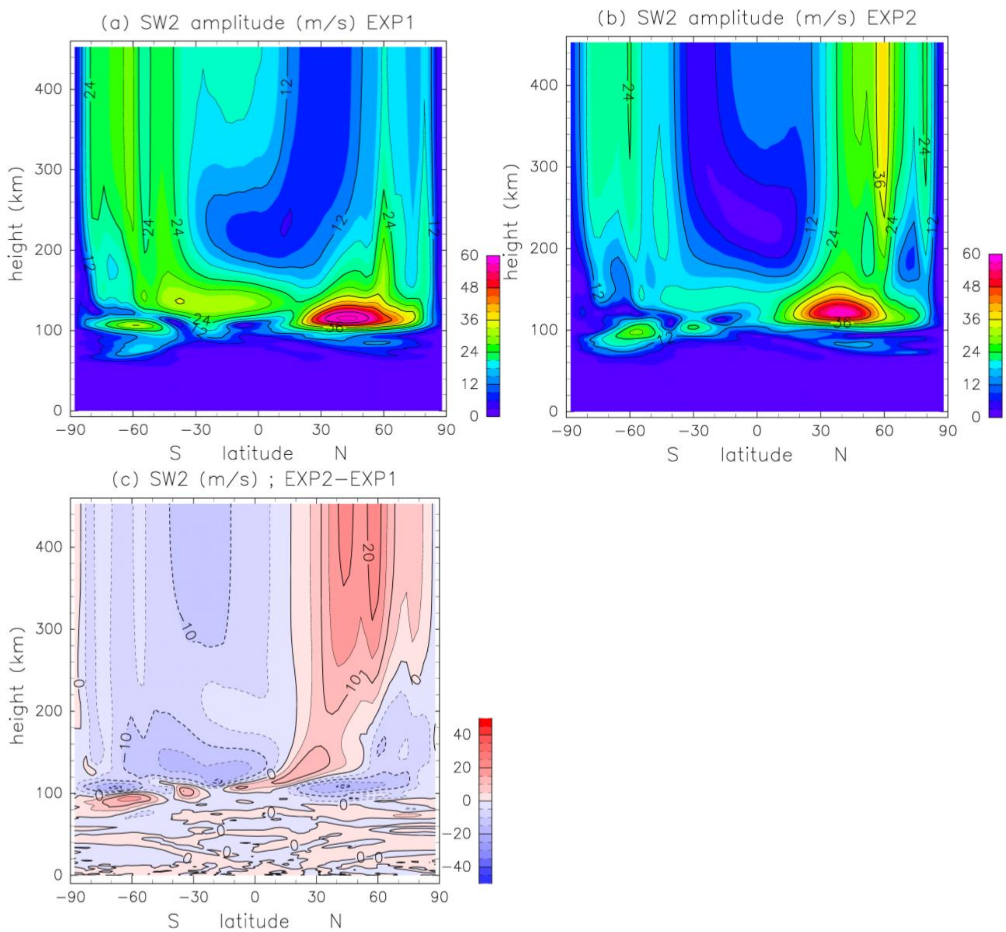

Figure3: (a) Height-latitude distribution of the zonal wind component of the SW2 amplitude in June obtained by EXP1. Units are m s^{-1}. Contour intervals are 6 m s^{-1}. (b) As in Figure 1a except for EXP2. (c) Zonal wind difference between EXP2 and EXP1 (EXP2–EXP1).

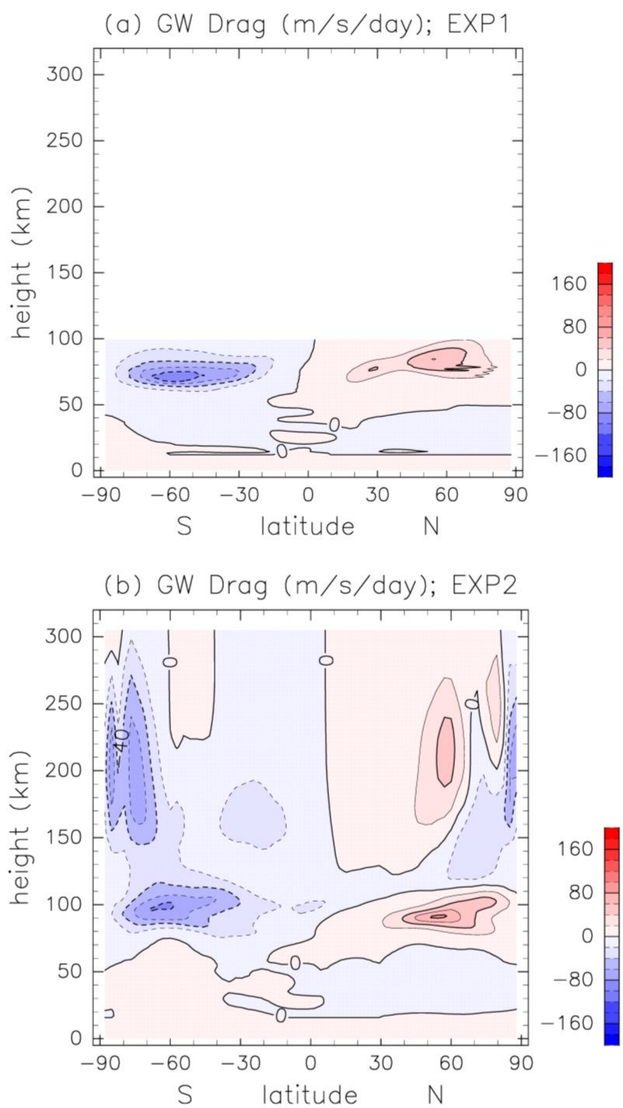

Figure 4: (a) Height-latitude section of the zonal mean of the zonal GW drag in June obtained by EXP1. Positive and negative values are eastward and westward acceleration, respectively. Units are m s^{-1} day^{-1}. (b) As in Figure 4a except for EXP2.

Ann. Geophys. Discuss., https://doi.org/10.5194/angeo-2019-36
Manuscript under review for journal Ann. Geophys.
Discussion started: 25 March 2019

Annales Geophysicae Discussions Open Access

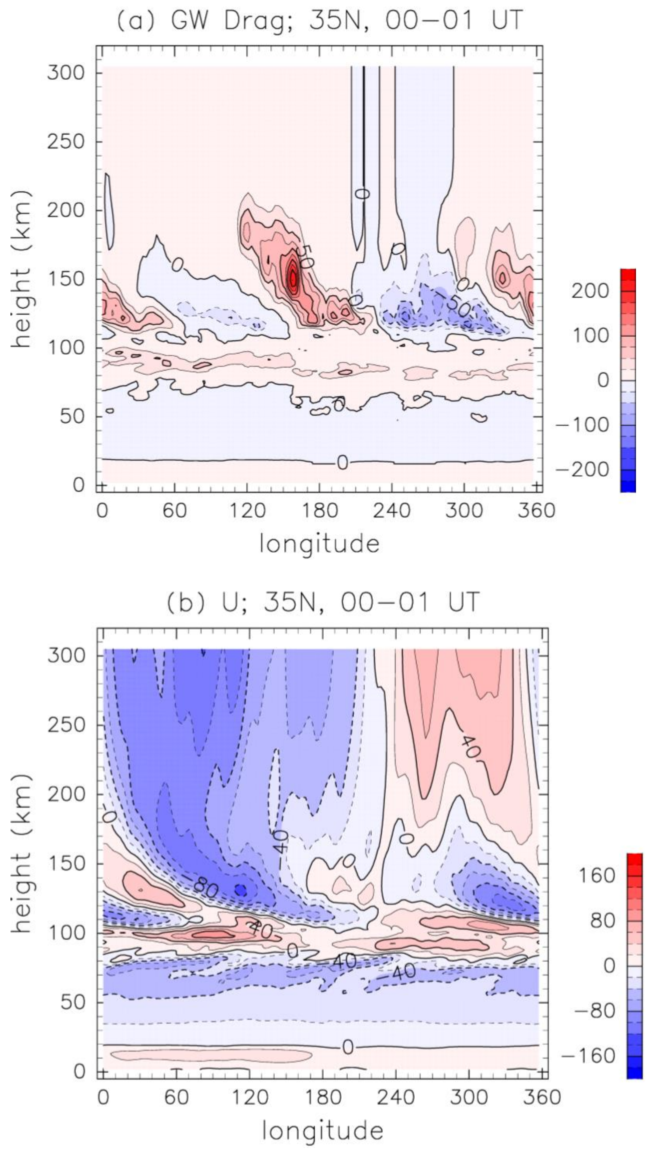

Figure 5: (a) Height-longitude section of the zonal GW drag at 35° N obtained by EXP2. Data are averaged between 00 UT and 01 UT in June. Units are m s^{-1} day^{-1}. (b) As in figure 5a except for zonal wind component. Units are m s^{-1}.

Ann. Geophys. Discuss., https://doi.org/10.5194/angeo-2019-36
Manuscript under review for journal Ann. Geophys.
Discussion started: 25 March 2019

Annales Geophysicae Discussions

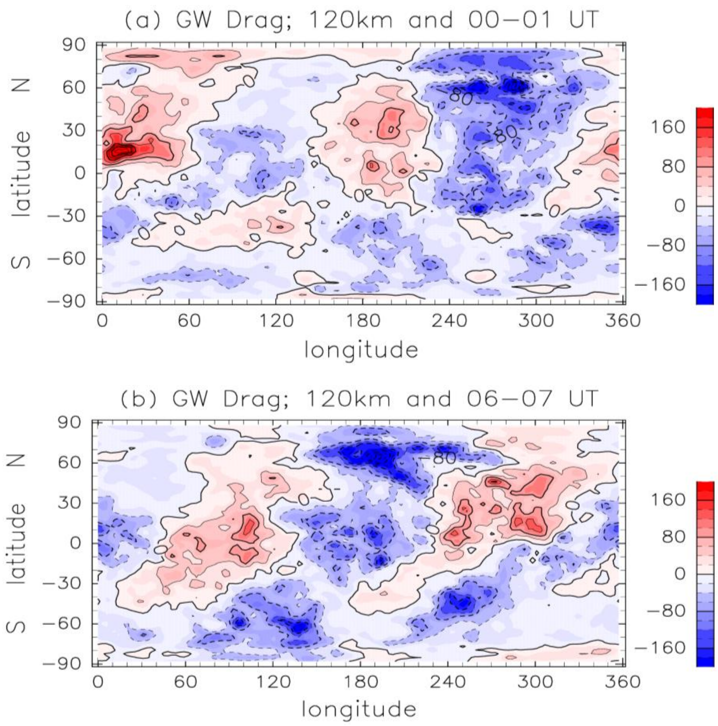

Figure 6: (a) Latitude-longitude section of the zonal GW drag at 120 km height in June. Data are averaged between 00 UT and 01 UT. Positive and negative values are eastward and westward acceleration, respectively. Units are m s^{-1} day^{-1}. Contour intervals are 40 m s^{-1} day^{-1}. (b) As in Figure 6a except for the average between 06 UT and 07 UT.

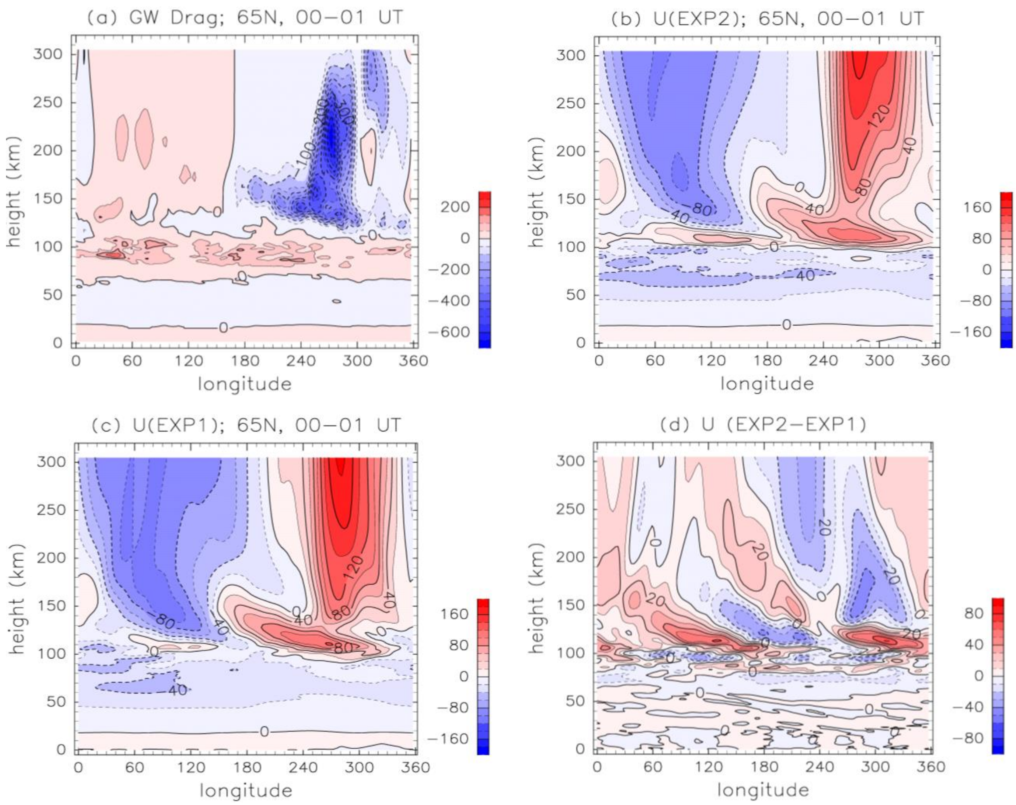

Figure 7: (a) Height-longitude section of the zonal GW drag at 65° N in June (EXP2). Data are averaged between 00 UT and 01 UT. Units are m s^{-1} day^{-1}. Contour intervals are 50 m s^{-1} day^{-1}. (b) As in figure 5a except for zonal wind component obtained by EXP2. Units are m s^{-1}. (c) As in Figure 7b except for EXP1. (d) Difference of zonal wind at 65° N between EXP2 and EXP1 (EXP2–EXP1). Units are m s^{-1}. Contour intervals are 10 m s^{-1}.

Ann. Geophys. Discuss., https://doi.org/10.5194/angeo-2019-36
Manuscript under review for journal Ann. Geophys.
Discussion started: 25 March 2019

Annales Geophysicae Discussions
Open Access

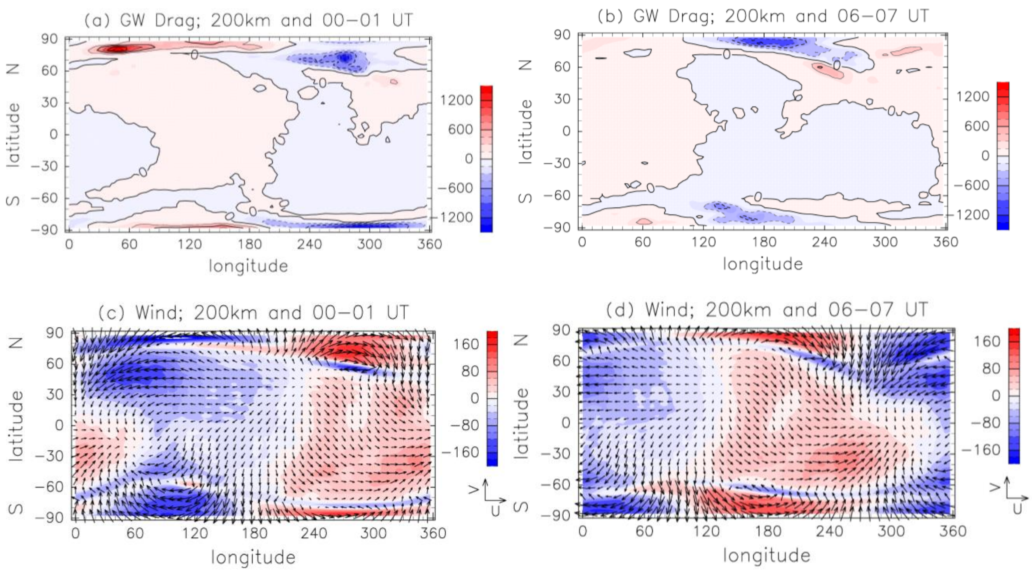

Figure 8: (a) Longitude–latitude section of the zonal GW drag at 200 km height in June. Data are averaged between 00 UT and 01 UT. Positive and negative values are eastward and westward acceleration, respectively. Units are m s^{-1} day^{-1}. Contour intervals are 200 m s^{-1} day^{-1}. (b) As in Figure 6a except for the average between 06 UT and 07 UT. (c) Vectors indicate the global distribution of the horizontal wind at 200 km height obtained by EXP2. Data are averaged between 00 UT and 01 UT in June. The vectors on the right-hand side indicate the zonal wind and meridional winds with magnitudes of 200 m s^{-1}. Color bars are the global distribution of the zonal wind component at 200 km height. Data are averaged between 00 UT and 01 UT. (d) As in Figure 8c except for the average between 06 UT and 07 UT.